JGR Atmospheres

RESEARCH ARTICLE
10.1029/2021JD035949

Trends in Downwelling Longwave Radiance Over the Southern Great Plains

Lei Liu[1], Yi Huang[1], John R. Gyakum[1], David D. Turner[2], and P. Jonathan Gero[3]

[1]Department of Atmospheric and Oceanic Sciences, McGill University, Montreal, QC, Canada, [2]NOAA/OAR/Global Systems Laboratory, Boulder, CO, USA, [3]Space Science and Engineering Center, University of Wisconsin–Madison, Madison, WI, USA

Key Points:

- Long-term downwelling longwave radiance observations reveal distinctive trends across the infrared spectrum
- Significant positive radiance trends in weak absorption bands indicate earlier detectability of climate change
- Radiance trend uncertainty mainly results from natural variability, emphasizing the need to continue the measurements

Correspondence to:
L. Liu,
lei.liu5@mail.mcgill.ca

Citation:
Liu, L., Huang, Y., Gyakum, J. R., Turner, D. D., & Gero, P. J. (2022). Trends in downwelling longwave radiance over the Southern Great Plains. *Journal of Geophysical Research: Atmospheres*, *127*, e2021JD035949. https://doi.org/10.1029/2021JD035949

Received 28 SEP 2021
Accepted 28 FEB 2022

Abstract Downwelling longwave radiation is an important part of the surface energy budget. Spectral trends in the downwelling longwave radiance (DLR) provide insight into the radiative drivers of climate change. In this research, we process and analyze a 23-year DLR record measured by the Atmospheric Emitted Radiance Interferometer (AERI) at the U.S. Department of Energy Atmospheric Radiation Program Southern Great Plains (SGP) site. Two AERIs were deployed at SGP with an overlapping observation period of about 10 years, which allows us to examine the consistency and accuracy of the measurements and to account for discrepancies between them due to errors associated with the instruments themselves. We then analyzed the all-sky radiance trends in DLR, which are associated with the surface warming trend at SGP during this same period and also the complex changes in meteorological conditions. For instance, the observed radiance in the CO_2 absorption band follows closely the near-surface air temperature variations. The significant positive radiance trends in weak absorption channels, such as in the wings of the CO_2 band and in the weak absorption channels in the H_2O vibration-rotational band, show earlier detectability of climate change. The magnitude of the radiance trend uncertainty in the DLR record mainly results from internal climate variability rather than from measurement error, which highlights the importance of continuing the DLR spectral measurements to unambiguously detect and attribute climate change.

1. Introduction

Longwave radiation is a key component of the atmospheric energy budget that drives climate change. At the top of the atmosphere (TOA), the outgoing longwave radiation (OLR), as well as its spectrally resolved radiance, is monitored by satellites with global coverage and long-term records (e.g., Liebmann & Smith, 1996; Stephens et al., 2012). This allows us to study changes in OLR and to test climate models (e.g., Brindley & Bantges, 2016; Harries et al., 2001; Huang & Ramaswamy, 2009; Huang, Ramaswamy, Huang, et al., 2007; Huang, Ramaswamy, & Soden, 2007; Palchetti et al., 2020; Pan et al., 2015; Wielicki et al., 2002). Even when there is continuous spatiotemporal coverage of OLR spectra, the compensating effects of greenhouse gas opacity and temperature warming make it difficult to detect climate change in satellite measurements (Huang, 2013; Huang & Ramaswamy, 2009).

Downwelling longwave radiation emitted by the atmosphere is one key component in the surface energy budget (Stephens et al., 2012; Trenberth et al., 2009). Compared to the radiation budget at the TOA, the surface radiation budget is more uncertain and longwave radiation is a main contributor to the uncertainty (Trenberth et al., 2009; Wild et al., 2012). This is largely due to the paucity of global and long-term downwelling longwave radiance (DLR) observations. Despite the limits of spectrally resolved DLR records, it has been demonstrated that DLR measurements are useful for understanding the surface energy balance and testing climate models. For example, Lubin (1994) explained the super greenhouse effect by using observed DLR spectra over equatorial oceans; Feldman et al. (2015) used the DLR spectra to measure CO_2 radiative forcing at the Southern Great Plains (SGP) and the North Slope Alaska sites; Huang et al. (2019), Kapsch et al. (2016), Shupe and Intrieri (2004), Sokolowsky et al. (2020) and several others diagnosed the DLR variability in relation to sea ice, clouds and other climate changes in polar regions.

Climate change is driven by changes in energy balance. This leads us to an overarching question regarding the surface energy balance: can climate change be detected and understood by monitoring the DLR spectrum? One advantage of the DLR, compared to the OLR, is that the compensating effects mentioned earlier vanish. In the

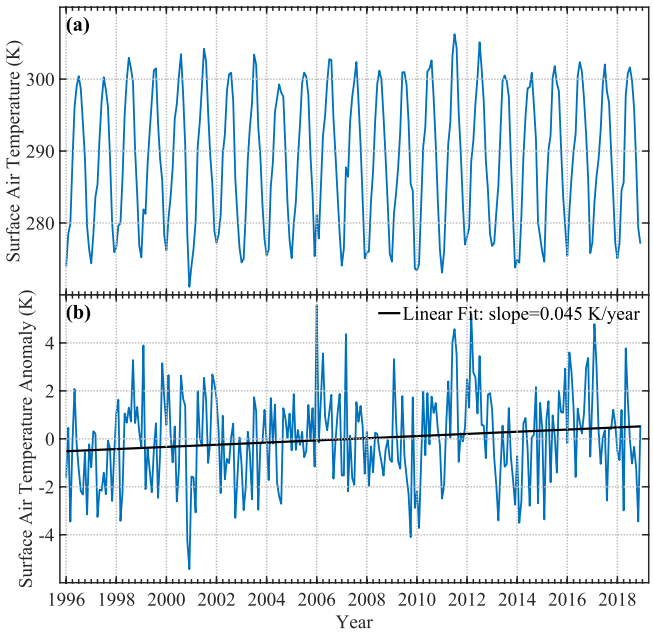

Figure 1. Warming trend at Southern Great Plains (SGP). Shown here is the ERA5 monthly mean 2 m air temperature time series at the SGP site (average of nine 0.25° × 0.25° resolution grid boxes centered at: 97.5°W and 36.5°N) between 1996 and 2018. The anomaly is defined with respect to multi-year monthly mean of each calendar month.

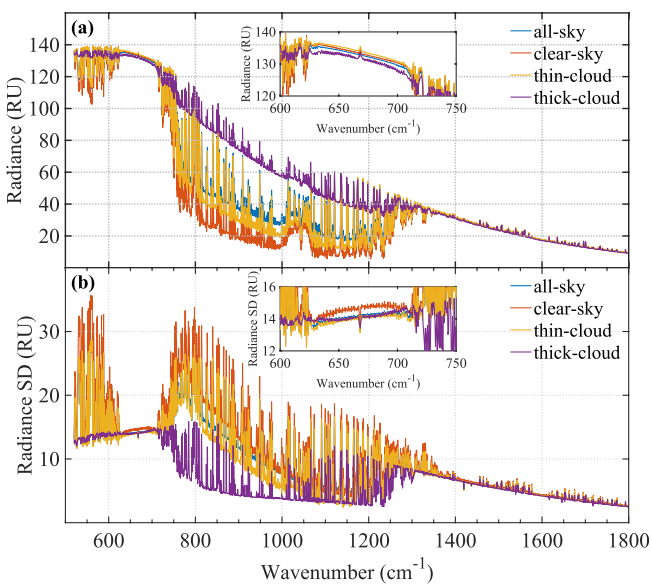

Figure 2. (a) Long-term average of all 23 annual mean AERI spectra for different sky conditions at Southern Great Plains (SGP). (b) Standard deviation of monthly mean AERI spectra for different sky conditions at SGP. (RU: Radiance Units; 1 RU = 1 mW/[m^2 sr cm^{-1}]) The insets in the two panels indicate the corresponding zoomed-in results in the CO_2 absorption band.

DLR, the greenhouse gas opacity and temperature warming effects reinforce each other to increase DLR. This makes DLR a potentially advantageous observation for monitoring climate change (Huang, 2013). The signals from different meteorological variables such as temperature, greenhouse gases, and clouds imprint different spectral signatures. This allows for a spectral fingerprinting of their changes (Huang et al., 2010). At the SGP site, the fifth generation European Centre for Medium-Range Weather Forecasts atmospheric reanalysis dataset, ERA5 (Hersbach et al., 2020), shows that there has been a significant warming in surface air temperature with a magnitude of ~0.045 K/year between 1996 and 2018 (Figure 1). Can this warming be detected from the DLR spectral records at that site?

We have two primary objectives in this paper. First, we are interested in constructing a long-term monthly DLR spectral record based on 23 years of measurements by the Atmospheric Emitted Radiance Interferometers (AERIs) installed at the U.S. Department of Energy Atmospheric Radiation Measurement (ARM) SGP site. Two AERIs have been deployed at this site and have rendered 10 years of overlapping observations but with different sampling strategies (i.e., 3 min sky average every 8 min vs. multiple 20-s sky average observations every 4 min). We will examine the accuracy and consistency of the measurements and assess them against synthetic spectra simulated from collocated atmospheric measurements using a benchmark radiation model. Second, we will analyze the combined long-term DLR spectral trends for the period of 1996–2018. We are interested in ascertaining if the radiance trends in the AERI bands dominated by near-surface emission are consistent with the warming temperature trend shown by ERA5 (Figure 1). This work will also test the veracity of the trends documented by Gero and Turner (2011) using the early years of the DLR record and analyze the contributions from different sky conditions.

2. Data and Methods

2.1. AERI Data Processing

The AERI is a ground-based Fourier transform spectrometer that measures the DLR emitted from the atmosphere with an accuracy of 1% ambient radiance at high temporal and spectral resolution (Knuteson et al., 2004a, 2004b). The measurements cover the spectral range between 520 and 3,020 cm^{-1} with a resolution of 0.5 cm^{-1}; however, we focus on the mid-infrared spectral range from 520 to 1800 cm^{-1} in this paper. Two high-emissivity blackbodies, a hot blackbody with a fixed temperature at 60°C and another blackbody at ambient temperature (Knuteson et al., 2004a), are used for radiometric calibration based on the method of Revercomb et al. (1988). The long-term average of all 23 annual mean DLR spectra and the standard deviation of monthly mean DLR spectra over the 23 years for different sky conditions at the SGP site are shown in Figure 2. We classify the scene into three different conditions: clear-sky, thin-cloud, and thick-cloud; the classification method will be explained in Section 2.2. The main difference in DLR between different sky conditions is primarily in the window portion of the spectrum (between 800 and 1200 cm^{-1}) shown in Figure 2a. The standard deviation of thick-cloud DLR is found to be the smallest among all the different sky conditions in the window band (Figure 2b), which indicates small variability of the radiating temperature of the thick clouds.

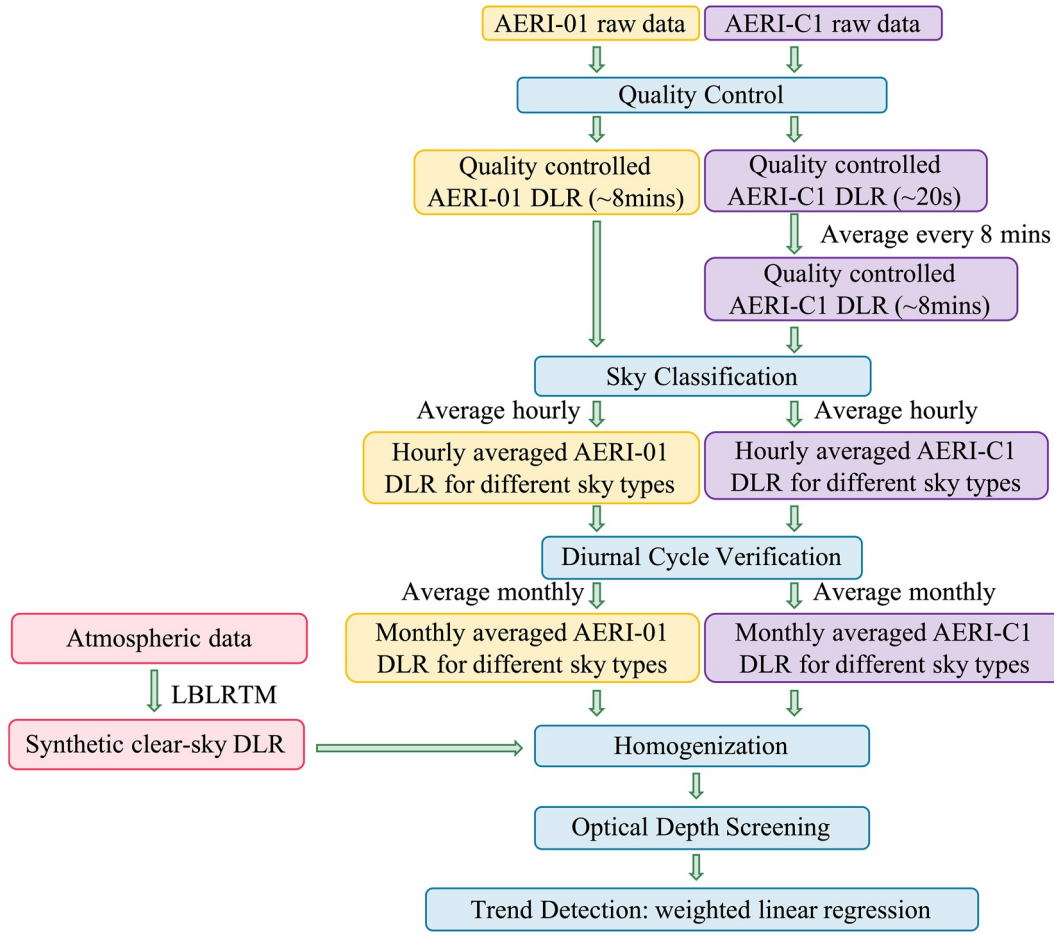

Figure 3. Data processing flowchart. Yellow and purple squares represent AERI-01 and AERI-C1 DLR data respectively. Blue squares represent important data processing steps. Pink squares represent radiative transfer model simulations. Details of processing steps are provided in the text.

The two AERIs deployed at SGP have different observational periods and different sampling frequencies. AERI-01 operated from July 1995 to March 2014, while AERI-C1 has operated from February 2004 to the present. C1 is the designator of the Central Facility location of the SGP site. Historically E14 was an alternate designator for the same location. AERI-C1 was named AERI-E14 before 2011, for example, in Gero and Turner (2011). The two AERIs were deployed side-by-side (within 5 m of each other). Given their vertical field of view (FOV) of 2.6° full-angle, both instruments view the same portion of the sky; 86% of the FOVs of the two AERIs are overlapped at the altitude of 1 km. The overlapping observations make it possible to test the accuracy and consistency of the measurements. However, the two instruments differ with respect to their sampling frequency. AERI-01 measures one DLR spectrum approximately every 8 min; its measurement cycle includes a 200-s sky-dwell period (Knuteson et al., 2004b) and the rest of the cycle is used for viewing the blackbodies for calibration. AERI-C1 uses a rapid mode with ~20-s sampling cycle (Turner et al., 2006). Such differences in the measurements necessitate appropriate procedures to homogenize the data from the two AERIs for inter-comparisons and trend analyses.

Figure 3 shows the flowchart illustrating the data processing adopted in this paper. First, rigorous quality control is performed on the data to retain reliable observations. During the long history of observations at the SGP site, many factors have caused errors including: contamination of the scene mirror, malfunction of the interferometer, and failure of the detector temperature sensor. We first discard all the erroneous data based on the AERI quality control reports from the ARM program (https://adc.arm.gov/discovery/#/results/instrument_class_code::aeri). In addition, similar to the quality control method described in Turner and Gero (2011), the hatch status and the sky view noise equivalent radiance tests are also implemented.

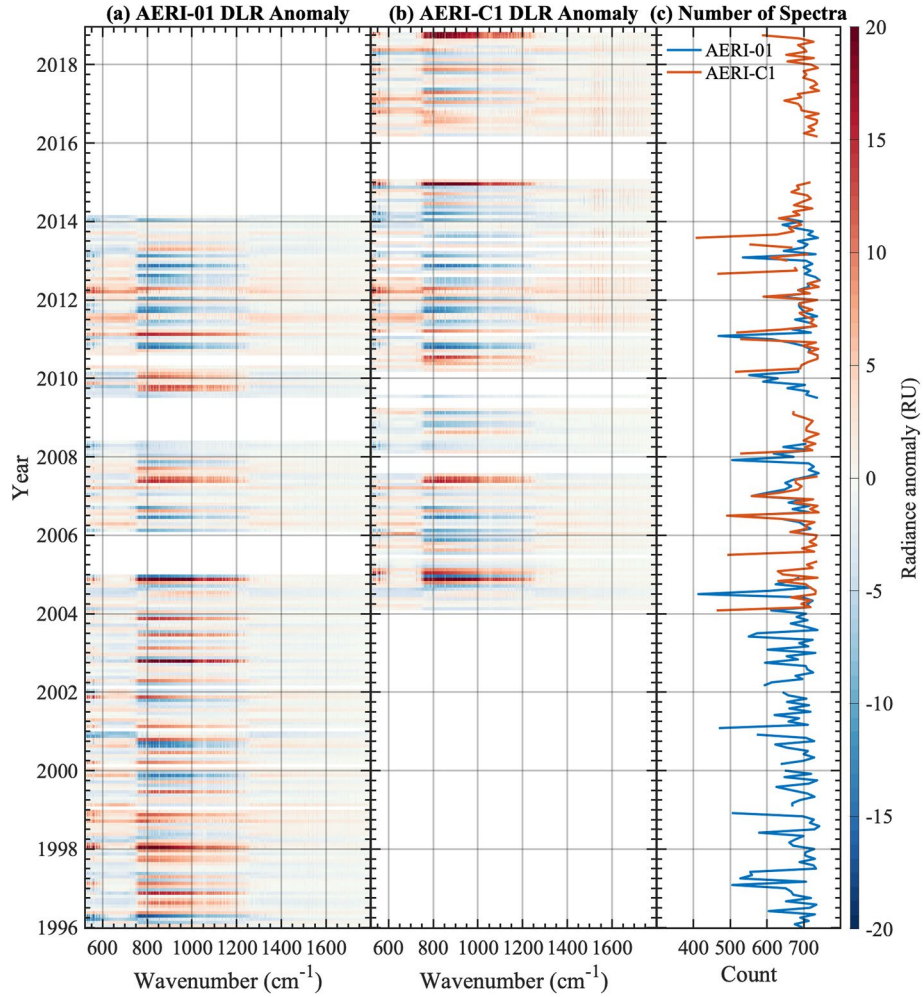

Figure 4. Monthly anomalies of AERI-observed downwelling longwave radiance spectra and hourly spectra count in each month.

After the *Quality Control* step, we average the AERI-C1 spectra over 8 min intervals, to be consistent with the AERI-01 sampling period. Then, in the *Sky Classification* step, we apply a machine learning algorithm (detailed in Section 2.2 below) to classify the sky conditions as one of clear, thin cloud, or thick cloud overhead based on the 8 min mean radiance spectra. Next, we compute averages of all 8 min spectra of each sky type within each hour and then average the hourly spectra of the same hour of the day to obtain a monthly averaged diurnal cycle. It is verified that there is uniform diurnal sampling in each month; no data of the 24-hr diurnal cycle is missing. Next, the monthly mean spectra are obtained by averaging the monthly averaged diurnal cycle. Monthly means are discarded when the count of hourly spectra is below 400 (~55%).

Some channels in the center of the CO_2 absorption band (~667 cm^{-1}) and the water vapor absorption band (1300–1800 cm^{-1}) for which the near-surface atmosphere is so opaque that the channels are essentially uncalibrated are discarded in the *Optical Depth Screening* step. These strongly opaque channels are identified using the criterion that the gaseous optical depth for a 1 m layer of atmosphere at the surface is above 0.5. Finally, the monthly anomaly spectra are obtained by subtracting from each monthly mean spectra the long-term average of all 23 monthly mean spectra for that calendar month (which effectively removes the seasonal cycle). These monthly anomaly time series are illustrated in Figure 4, and are used in the following analyses and figures. The long-term trends in the DLR monthly mean spectra are analyzed based on the monthly anomaly spectra. Synthetic clear-sky DLR, computed using collocated radiosonde data and a radiative transfer model (described below),

are used as a baseline to evaluate the measurements of the two AERIs during the overlapping period; details are provided in Appendix A.

Both AERIs produced more than 600 hourly mean spectra per month nearly 90% of the time (Figure 4c). The strongest monthly DLR anomalies are seen in the window band (800–1200 cm^{-1}; Figures 4a and 4b). The pattern of the DLR anomalies in the overlapping observational period is similar in both AERI-01 and AERI-C1.

2.2. Sky Classification

Clouds strongly influence the DLR spectra, especially in the atmospheric window (800–1200 cm^{-1}). In order to identify the causes of the DLR trends, we separate the clear-sky spectra from the cloudy cases and examine their trends separately.

A sky-classification model is developed using a machine-learning method based upon the k-nearest neighbor (k-NN) algorithm (Cunningham & Delany, 2020). The 8 min AERI-01 and AERI-C1 spectra for the period between 1 March 2011 and 31 July 2012 are used to train the k-NN model. We use the same inputs and truth data from Raman Lidar as in Turner and Gero (2011). The k-NN classification achieves an accuracy of 94.8%. This algorithm determines the sky to be *clear* or *cloudy*, while the cloudy sky is then further classified to be *thin-cloud* when 70 min averaged 985 cm^{-1} brightness temperature is lower than 250 K; otherwise, it is classified to be *thick-cloud*. We also tried a classical backpropagation gradient-descent classification algorithm as used by Turner and Gero (2011), which achieves an accuracy of 90%. The resulting trends are not sensitive to the classification method chosen. The results presented below are based on the k-NN algorithm.

Based on the classification of *thin-cloud* and *thick-cloud*, the *thick-cloud* emitting temperature range is smaller than that for *thin-cloud*, primarily because *thick-clouds* are opaque clouds relatively close to the surface while *thin-cloud* may be either partially cloudy scenes or clouds higher in the troposphere. This is why the *thick-cloud* classification has the smallest standard deviation of DLR among the three different sky conditions.

2.3. Homogenization

During the overlapping observational period, discrepancies larger than the documented AERI absolute calibration uncertainty (Knuteson et al., 2004a) were observed between the monthly mean spectra observed by AERI-01 and AERI-C1. Large radiance discrepancies occur, especially in the window band, and are found to mainly come from clear-sky scenes (see Figure B1 and discussions in Appendix B). This suggests that the discrepancies likely result from calibration (Rowe, Neshyba, Cox, & Walden, 2011; Rowe, Neshyba, & Walden, 2011) and other undetected errors (e.g., something in the FOV of one instrument but not the other). In order to avoid discarding meaningful data in the trend analysis, we simulate the clear-sky DLR spectra using a radiation model together with collocated atmospheric measurements and use these synthetic spectra as a reference to assign proper weights in combining the data of AERI-01 and AERI-C1, based on the findings of previous radiance closure studies (e.g., Turner et al., 2004) that demonstrated high accuracy in such synthetic spectra.

The radiation model used here is the Line-by-Line Radiative Transfer Model (LBLRTM v12.9; Clough et al., 2005). To compute the clear-sky DLR spectra at SGP, we use the temperature and water vapor profiles from the ARM Balloon-Borne Sounding System (https://www.arm.gov/capabilities/instruments/sonde). The water vapor mixing ratio profiles derived from radiosondes are scaled with a height-independent factor to match the precipitable water vapor (PWV) retrieved by the microwave radiometer at the SGP site. This approach has been used to compensate for the dry-bias issue found in the radiosonde water vapor data (Holdridge, 2020; Revercomb et al., 2003; Turner et al., 2003; Wang et al., 2002). CO_2 and CH_4 concentration profiles are obtained from the CarbonTracker website (http://carbontracker.noaa.gov, Jacobson et al., 2020; Peters et al., 2007). O_3 concentration profiles are adjusted from NASA's Modern-Era Retrospective analysis for Research and Applications, Version 2 (MERRA-2, Gelaro et al., 2017) ozone product to get a better radiative closure with AERI-observed DLR (see more details in Appendix B). We use a 200-level input profile for the LBLRTM simulations. The first and second levels are at 0 and 10 m above ground level respectively. The depth of each subsequent layer is increased by 2% relative to the one below.

As radiosonde observations of near-surface layers are essential to the DLR spectra, the AERI data are selected to match the radiosonde launch time. We keep the spectra whose observation time is within 10 min of the radiosonde launch time. For each month, about 70 clear-sky DLR spectra are simulated on average. The absolute values of the radiance biases (R_{bias}) are determined as the monthly mean radiance differences between the synthetic and observed DLR spectra.

During the overlapping observational period, the monthly mean AERI-01 and AERI-C1 DLR spectra are combined according to Equation 1 and Equation 2 using the ratio r, which represents the proximity of the AERI's observed DLR spectra to the synthetic DLR spectra. r is a function of wavenumber. The 5th, 50th and 95th percentiles of the ratio r across all AERI channels over the 23-year period are 0.55, 2.06, and 12.84 respectively. The weighted radiance used in the trend analysis is given by Equation 2, where $R_{AERI-01}$ and $R_{AERI-C1}$ represent the observed AERI-01 and AERI-C1 monthly mean DLR respectively.

$$r = \frac{R_{bias(AERI-01-LBLRTM)}}{R_{bias(AERI-C1-LBLRTM)}} \tag{1}$$

$$R = R_{AERI-01} \times \frac{1}{1+r} + R_{AERI-C1} \times \frac{r}{1+r} \tag{2}$$

2.4. Trend Detection

A weighted linear regression method is applied to determine if there are any trends in the observed DLR. We develop our weighted linear regression model based on the regression model developed by Tiao et al. (1990) and Weatherhead et al. (1998).

This model determines the radiance trend, $\hat{\omega}$ in each AERI channel, as:

$$\hat{\omega} = \frac{\sum_{t=1}^{T} W_t \left(t - \bar{t}\right) y_t^{\star}}{\frac{1-\phi}{12} \sum_{t=1}^{T} W_t \left(t - \bar{t}\right)^2} \tag{3}$$

In Equation 3, T represents the total number of months and $\bar{t}$ represents the mean value of t. ϕ is the autocorrelation in the noise of the time series considering a first-order autoregressive (AR1) process, and $y_t^{\star}$ represents the transformed radiance anomalies (see Figure A1) after removing the effect of the AR1 process (see details in Appendix A). W_t represents the weights which are determined as the intra-month variability of the all-sky observed DLR, shown in Equation 4:

$$W_t = \frac{N_t}{{\sigma_t}^2} \tag{4}$$

where N_t and ${\sigma_t}^2$ represent the number and variance of hourly observations in each month. Large variability of DLR results in smaller weights. We use the same weights for all sky conditions.

Along with the magnitude of the trend it is also important to determine the associated uncertainty, $\sigma_{\hat{\omega}}$, which is shown in Equation 5. In Equation 5, ${\sigma_N}^2$ and ${\sigma_e}^2$ represent the variance of the error due to internal variability in the time series and the variance of the measurement error respectively. Here, we mainly account for two sources of uncertainty. First, there is the uncertainty arising from internal climate variability. This is accounted for by the term in Equation 5 associated with σ_N and ϕ. Second, there is the uncertainty arising from instrumentation errors accounted for by the term in Equation 5 associated with σ_e. We use the radiance difference between clear-sky LBLRTM simulation and clear-sky AERI-observation as the measurement error. We assume that these two sources of uncertainty are independent of each other. The derivation of Equation 5 is given in Appendix A.

$$\sigma_{\hat{\omega}} = \frac{12\sqrt{\sum_{t=1}^{T} W_t^2 \left(t - \bar{t}\right)^2}}{\sum_{t=1}^{T} W_t \left(t - \bar{t}\right)^2} \sqrt{{\sigma_N}^2 \frac{1+\phi}{1-\phi} + {\sigma_e}^2} \tag{5}$$

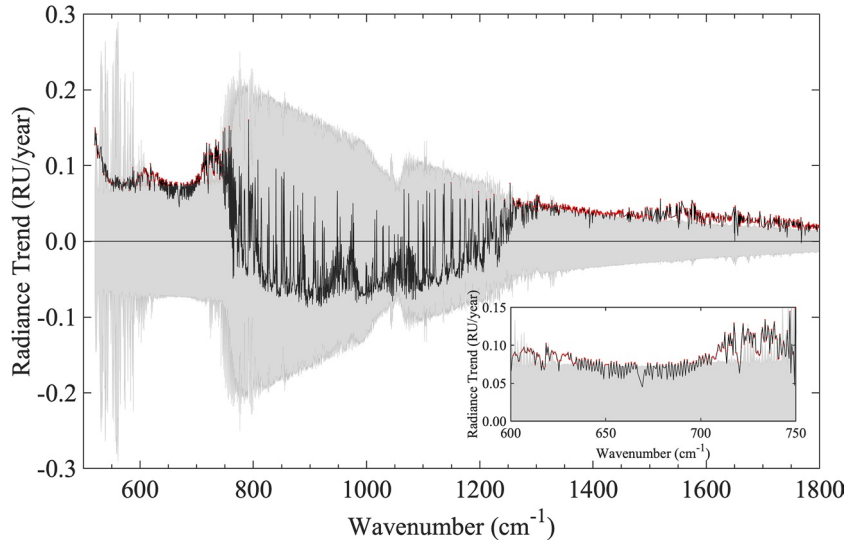

Figure 5. The all-sky radiance trends. The spectral elements indicated with red dots have trends that exceed the 95% significant test. The shading in the figure is the 95% confidence interval. The inset shows the zoomed-in results of CO_2 absorption band.

The derived $\sigma_{\hat{\omega}}$ in Equation 5 is referred to as the standard error of the trend magnitude. It is used to test whether the trends deviate significantly from 0 at the 95% significance level. A trend is considered to be significant at the 95% significance level if the trend magnitude is larger than $2\sigma_{\hat{\omega}}$. In following figures, the uncertainty envelope plotted in gray corresponds to the 95% confidence interval.

3. Results

3.1. All-Sky Radiance Trends

The homogenized DLR records have been constructed, based on monthly averaged AERI-01 data from 1996 to 2013 and AERI-C1 data from 2004 to 2018. In total, we have 23 years of DLR data at SGP for analysis.

It can be inferred from the monthly anomalies shown in Figure 4 that the DLR trends depend on the analysis period as the anomalies do not show monotonic changes over this 23-year period. The AERI-01 data (Figure 4a) show more frequent negative anomalies after 2011 in the window band (800–1200 cm^{-1}), which is consistent with the negative trends reported in Gero and Turner (2011) for this instrument. However, including AERI-C1 data (Figure 4b) affords a longer DLR spectral record, and the latest several years are characterized by warm anomalies.

The long-term all-sky radiance trends during the 1996–2018 period are shown in Figure 5. The all-sky DLR trends have different features in different spectral regions. In the CO_2 absorption band centered around 667 cm^{-1}, the trends are generally positive (i.e., radiance is increasing over time) and are statistically significant in the band wings but not at the center. In the window band (800–1200 cm^{-1}), there are very few statistically significant trends. In the water vapor absorption band (1300–1800 cm^{-1}), similar to the CO_2 absorption band, the radiance trends are generally positive and statistically significant.

DLR in different AERI channels are controlled by different meteorological variables. To illustrate this point, Figure 6a shows the correlation coefficients between the deseasonalized and detrended monthly anomalies in the radiance (brightness temperature) spectra from the two AERIs and surface air temperature from ERA5. Note that AERI-01 and AERI-C1 have different observational periods, which result in different correlation coefficients especially in the window band. In the center of the CO_2 absorption band (667 cm^{-1}) and channels corresponding to strong H_2O absorption lines, the correlation coefficient is close to one, indicating that the variance in the radiance in these channels is primarily controlled by the surface air temperature. This is because the atmospheric

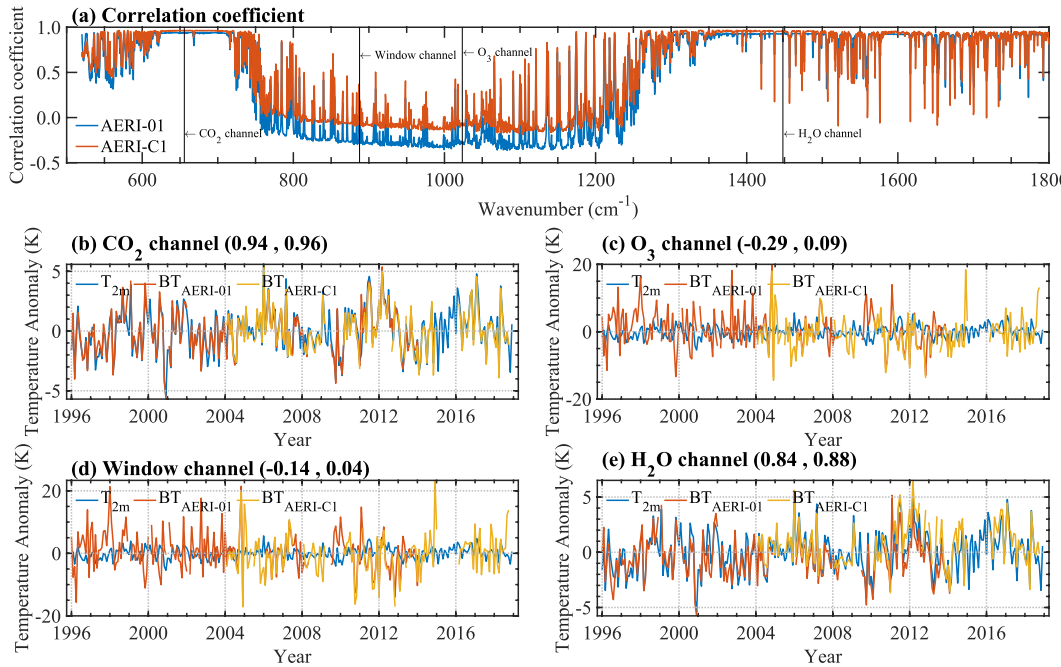

Figure 6. (a) The correlation coefficient between the AERI-observed brightness temperature spectra and near-surface air temperature from ERA5 at the SGP site over the 23-year period. (b–e) The time series of the deseasonalized brightness temperature and near surface air temperature in four AERI channels. In each title, the values in the parentheses are the correlation coefficients between near-surface air temperature from ERA5 and observed brightness temperature by AERI-01 and AERI-C1, respectively.

absorption is strongly saturated in these channels and thus they are less sensitive to variations in the concentrations of the gases themselves and to temperatures of the atmospheric constituents farther removed from the surface. In comparison, in the wings of the CO_2 band and the weaker H_2O absorption lines, the atmospheric absorption is not saturated so that variability in DLR is subject to the variation in the temperature and gas concentration throughout the vertical column. This means that the trends both in temperature and gas concentrations drive the radiance to increase, which explains the stronger and statistically more significant trend signals in these channels, as seen in Figure 5.

In Figure 6, the time series of the brightness temperature in four selected AERI channels: a CO_2 channel at 655.72 cm^{-1}, a window channel at 887.63 cm^{-1}, a O_3 channel at 1023.60 cm^{-1}, and a H_2O channel at 1447.89 cm^{-1} (Figures 6b–6e) are displayed. There is good consistency between the AERI-01 and AERI-C1 observed brightness temperature in all four channels. The all-sky brightness temperature at the CO_2 channel follows closely with the surface air temperature from ERA5 (Figure 6b). The near-surface warming of 0.045 K/year (Figure 1) is equivalent to 0.071 RU/year at this channel, which is close to the observed all-sky radiance trend of ~0.072 RU/year (averaged trend between 5 nearby channels). In the H_2O channel, the brightness temperature measured by the AERIs also follows the near surface air temperature (Figure 6e) but not as closely as the CO_2 channel (Figure 6b). In contrast, the brightness temperature anomalies in the window and O_3 channels have larger fluctuations than that in the CO_2 and H_2O channels and are evidently decoupled from the near surface air temperature (Figures 6c and 6d).

That the radiance trend is reinforced by both warming and opacity effects in the weak absorption channels indicates the benefits of using these AERI measurements in climate change detection. Assuming the trend magnitude and uncertainty determined from this 23-year record remain unchanged into future, the years to detect a significant trend, $n^{\star}$, at 90% significance level is:

$$n^{\star} \approx \frac{3.3\sigma_{\hat{\omega}}}{|\hat{\omega}|} \times 23\ years \tag{6}$$

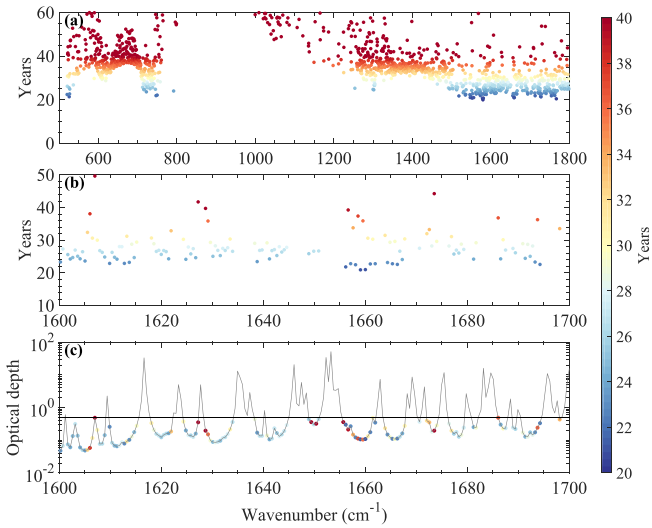

Figure 7. Trend detectability. (a) Time to detect (T2D) radiance trends at 90% significance level in different AERI channels; in comparison, the T2D for the 2 m temperature from the ERA5 reanalysis is about 30 years. (b) Zoomed-in figure of panel (a) in the water vapor absorption band. (c) The T2D (color-coded), in relation to atmospheric absorption strength, measured by the optical depth of a 1 m-thick atmospheric layer near the surface. The horizontal line marks optical depth of 0.5.

where $\hat{\omega}$ is the 23-year trend determined by Equation 3 and $\sigma_{\hat{\omega}}$ is the trend uncertainty determined by Equation 5. The derivation of Equation 6 is given in Appendix A.4. Although the trends are considered significant when $|\hat{\omega}| > 2\sigma_{\hat{\omega}}$, we require $|\hat{\omega}| > 3.3\sigma_{\hat{\omega}}$ when computing $n^{\star}$. As discussed in Appendix C, this yields a more conservative estimation of $n^{\star}$ compared to the method of Leroy et al. (2008).

Based on this equation, approximately 30 years are needed to detect a significant trend in the 2 m air temperature from the ERA5 data shown in Figure 1 when $\hat{\omega}$ and $\sigma_{\hat{\omega}}$ are substituted with the 2 m air temperature trend magnitude and trend uncertainty, respectively. In comparison, Figure 7 shows earlier detectability of the radiance trends in weak absorption channels, such as in the wings of the CO_2 band and in the weak absorption channels in the H_2O vibration-rotational band. In Figure 7c, the earlier detectability of the radiance trends in the H_2O vibration-rotational band is noticeable in the wings of strong absorption lines (i.e., where the optical depth is relatively lower). We can conclude that it is advantageous to monitor the DLR in these weaker-absorption channels for climate change detection.

Trend detection in the radiance record is determined by comparing the trend signal to the uncertainties arising from different causes. Here, based on Equation 5, we account for uncertainties arising from climate internal variability (σ_N) and also instrumentation error (σ_e; Figure 5). The overall uncertainty is notably large in the window band for the all-sky condition (Figure 5), which impedes the detection of any significant radiance trends in this especially variable spectral region. Analysis of the respective parameters in Appendix A (see Figure A2) indicates that internal climate variability dominates instrumentation error when shaping the overall uncertainty envelope in Figure 5. It is also found that the influence of the autoregressive process does not strongly influence the trend uncertainty, as evident by the small value of ϕ, especially in the window band (Figure A2). We conclude that the trend uncertainty mainly arises from internal climate variability.

3.2. Trends in Different Cloud Conditions

The results presented in the previous subsection demonstrate that the radiance trends in the window band are different from the greenhouse gas absorption bands; the window band is also prone to high levels of uncertainty due to the marked variability of the signal that ranges from small values in clear sky conditions to large values when opaque low-altitude clouds are overhead. Given the fact that clouds are a significant factor that influences this band (see Figure 2), we analyze the radiance trends under different cloud conditions in this subsection.

The fraction of time that each sky condition occurs in 1 month (referred to as "sky fraction") based on the hourly spectra are shown in Figure 8. First, there is a good agreement between AERI-01 and AERI-C1 in the sky fraction monthly time series, with correlation coefficients of 0.94, 0.89, and 0.94 for clear-sky, thin-cloud, and thick-cloud, respectively. The clear-sky fraction between June 1996 and May 2010 from our classification is around 42% which is comparable to what was found by Turner and Gero (2011).

The clear-sky fraction increases at a rate of $0.17 \pm 0.09\%$ per year, while the thick-cloud fraction decreases at a rate of $-0.18 \pm 0.09\%$ per year. There is no significant trend for thin-cloud fraction. Understanding the atmospheric mechanisms that drive the trends in the sky fraction for different sky conditions are the subject of investigation in a future work.

Trends in AERI-observed DLR for different sky conditions based on the k-NN classifier are shown in Figure 9. In the window band, the clear-sky and thin-cloud trends are positive, while the thick-cloud trends are negative; however, none of those trends are statistically significant from zero because of the notably large trend uncertainty. The positive trend in the window band in the clear-sky data is likely due to increases in PWV, as hypothesized by Gero and Turner (2011). The positive trend in the thin-cloud classification suggests that either the clouds in

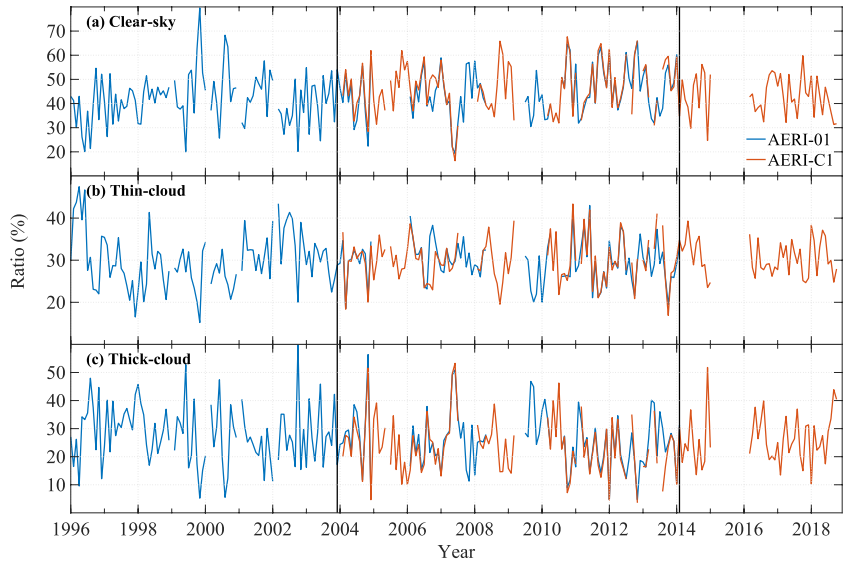

Figure 8. The monthly sky fractions of different sky conditions, categorized based on 8 min mean spectra at the Southern Great Plains site. The overlapping observational period is between the two vertical thick black lines.

these scenes are becoming more opaque, the clouds are becoming warmer (perhaps by moving lower in the troposphere), the PWV is increasing, or some combination of the three. The decrease in the thick-cloud trend in the window suggests that these thicker clouds are either becoming cooler or moving higher in the troposphere. In the spectral regions outside the window band, the trends for different sky conditions are generally positive and have the same features as the all-sky scenes.

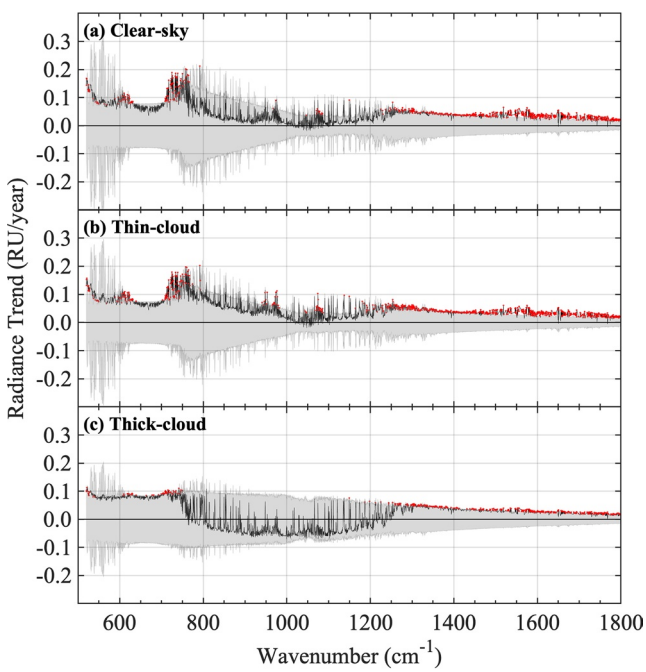

Figure 9. The trends in AERI-observed downwelling longwave radiance for different sky conditions at the Southern Great Plains site. The spectral elements marked with red dots indicate that the trends pass the 95% significance test. The shading in the figure is the 95% confidence interval.

The all-sky DLR trends are caused by changes in both sky fraction and the radiance of each sky condition. We use Equation 7 to separate the contributions from these factors, in which R_{all} represents the all-sky radiance, f_i and R_i represent the sky fraction and mean radiance for different sky conditions.

$$\frac{dR_{all}}{dt} = \sum \frac{df_i}{dt} R_i + \sum \frac{dR_i}{dt} f_i + residual \tag{7}$$

The results of the decomposed trends based on Equation 7 are shown in Figure 10. The small residual term (purple line in Figure 10a), which comes from nonlinear effects, suggests that the overall all-sky radiance trends can be well explained by Equation 7. In the window band, the overall radiance trends are a result of the compensation between the sky fraction change (orange line in Figure 10a) and the radiance change (yellow line in Figure 10a). In the opaque portions of the CO_2 absorption band (centered at 667 cm^{-1}) and H_2O absorption band (1300–1800 cm^{-1}), the overall radiance trends are caused by radiance change which is due almost entirely to the increases in the near-surface temperature because the atmosphere is already too opaque to reflect any gas concentration changes.

The overall radiance trends caused by sky fraction changes (orange line in Figure 10a) are a result of the compensation between changes in the clear-sky (blue line in Figure 10b) and the thick-cloud fraction (yellow line in Figure 10b) except in the opaque regions of the CO_2 absorption band (centered at 667 cm^{-1}) and H_2O absorption band (1300–1800 cm^{-1}). In the CO_2 absorption band and H_2O absorption band, the perfect compensation between positive trends caused by clear-sky and thin-cloud sky fraction changes and the negative trends caused by thick-cloud sky fraction changes

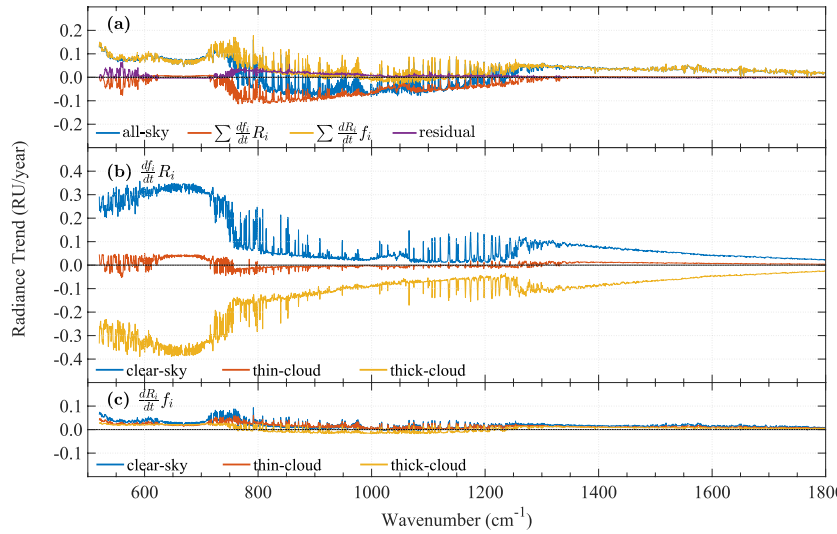

Figure 10. The all-sky downwelling longwave radiance (DLR) trends decomposed into the contributions from the sky fraction and radiance changes of different sky conditions. (a) The blue line represents the calculated all-sky DLR trends, which is the same as that from Figure 5. The orange and yellow lines represent the contributions from sky fraction change and radiance change determined using Equation 7, respectively. The purple line is the residual term from Equation 7; (b) The all-sky DLR trends caused by sky fraction change. The blue, orange, and yellow lines represent the contributions from clear-sky, thin-cloud, and thick-cloud fraction changes respectively; (c) The all-sky DLR trends caused by radiance change. The blue, orange, and yellow lines represent the contributions from clear-sky, thin-cloud, and thick-cloud radiance changes respectively.

results in almost no trends. In the window band, the negative trends are mainly caused by the thick-cloud fraction change.

In the window band (800–1200 cm^{-1}), the overall radiance trends caused by radiance change (yellow line in Figure 10a) result from the compensation between positive clear-sky and thin-cloud radiance change trends and negative thick-cloud radiance change trends (Figure 10c). By contrast, in the CO_2 absorption band (centered at 667 cm^{-1}) and H_2O absorption band (1300–1800 cm^{-1}), the radiance changes for the three sky conditions all contribute similarly to the overall radiance trends caused by radiance change.

4. Discussion and Conclusions

In this study, a long-term record of DLR at the SGP site has been constructed for analyzing the DLR trends, based on a weighted linear regression method that takes into account both natural climate variability and measurement error. Compared to previous studies, our analysis is based on a longer DLR record combined from the two AERIs at the SGP site, and makes use of synthetic DLR data in validating and differentiating the AERI measurements over their overlapping observational period. In addition, we quantitatively decompose the overall radiance trends due to the contributions from sky fraction change and the radiance change in each of these sky conditions.

The trends in DLR in different spectral ranges have different features. The trends are generally positive in the CO_2 and H_2O absorption bands, while no statistically significant trends are detected in the window band (Figure 5). We find that in the more opaque regions (the center of the CO_2 and H_2O absorption bands), the radiance is controlled by the near-surface air temperature (Figure 6) because of the strong atmospheric absorption. The sensitivity of DLR to near-surface air temperature indicates the potential of DLR to monitor climate change. In the wings of these absorption bands, both the near-surface atmospheric warming and the increase of the abundance of these trace gases contribute to the radiance trends (Feldman et al., 2015), which makes a climate trend signal more readily detectable, as hypothesized by Huang (2013). In the window band, the radiance is decoupled from the near-surface air temperature (Figure 6) because of the impact of sky-fraction changes of different scenes (clear and cloudy-skies).

We find that the sky-fraction change and the radiance change led to compensating effects on the DLR trends. This compensation results in weakly (statistically insignificant) negative radiance trends in the window band (Figure 10). In contrast, the radiance trends are dominated by the radiance change in the CO_2 and H_2O absorption bands, which are similar in all three sky conditions.

The influences of both natural climate variability and measurement error are considered when determining the uncertainty of the trend magnitude (Equation 5, Figure A2). We find that for all sky conditions, the majority of the uncertainty comes from the natural variability. This underlines the necessity of continuous DLR measurements to ascertain the DLR trends, especially in the window band (Figure 5).

The two AERIs at the SGP site provide us with an excellent opportunity to test the accuracy and consistency of the instruments. The discrepancies between the two AERIs in the overlapping periods may have come from calibration error and other undetected instrumentation errors. In this study, we use synthetic data to differentiate and combine the two AERIs' observations. Further investigation is required to understand the origin of the discrepancies and therefore to assure the measurement accuracy.

This paper has focused on the detection, as opposed to attribution, of the DLR trends. In the clear-sky case, atmospheric temperature and radiative gas concentration changes (primarily water vapor) are likely the main contributors to the DLR changes. As for the cloudy-sky case, changes in both the atmospheric states and cloud properties may contribute to the DLR changes. Future work is warranted to understand and quantitatively attribute the DLR trends disclosed in this paper to different meteorological variables.

Appendix A: Trend Detection

We first summarize the linear trend model and trend estimation from Tiao et al. (1990) and Weatherhead et al. (1998) in A.1 and A.2. We adopt the notation in their papers. Then we add the measurement error term to the trend detection in A.3 following Tiao et al. (1990).

A.1. Basic Linear Trend Modeling

In order to detect a linear trend, we first construct a simple model that describes the monthly mean radiance Y_t as:

$$Y_t = \mu + S_t + \omega X_t + N_t, t = 1, \cdots, T \tag{A1}$$

where μ is a constant term, S_t represents the seasonal component, ω is the trend magnitude to be determined, $X_t = \frac{t}{12}$ represents time measured in the units of year, N_t represents the unexplained portion of the data (i.e., the noise), and T represents the length of the data set in months.

The seasonal component S_t is determined by computing a long-term average of each calendar month. This component is subsequently removed from the monthly mean.

$$y_t = Y_t - S_t = \mu + \omega X_t + N_t, t = 1, \cdots, T \tag{A2}$$

The noise N_t is assumed to be autoregressive of the order of 1 (AR1):

$$N_t = \phi N_{t-1} + \epsilon_t \tag{A3}$$

where ϵ_t is assumed to be random white noise with zero mean and common variance $\sigma_\epsilon{}^2$, $\epsilon_t \sim W\left(0, \sigma_\epsilon{}^2\right)$. The autocorrelations in the noise come from various natural factors. ϕ is determined as the autocorrelation coefficient of the AR1 process after removing from y_t a linear trend component obtained by regressing y_t to time using a simple weighted linear least squares method (i.e., neglecting the AR1). The all-sky ϕ is shown in Figure A2a.

The variance of the noise N_t can also be determined from the detrended y_t time series:

$$\begin{aligned}\sigma_N{}^2 &= Cov(N_t, N_t) = Cov(\phi N_{t-1} + \epsilon_t, \phi N_{t-1} + \epsilon_t)\\ &= \phi^2 Cov(N_{t-1}, N_{t-1}) + Cov(\epsilon_t, \epsilon_t)\\ &= \phi^2 \sigma_N{}^2 + \sigma_\epsilon{}^2\end{aligned} \tag{A4}$$

Thus,

$$\sigma_N{}^2 = \frac{\sigma_\epsilon{}^2}{1-\phi^2} \tag{A5}$$

A.2. Trend Estimation With Weights

Given ϕ, to obtain the trend estimation, we consider a transformed model:

$$\begin{aligned}y_t{}^\star &= y_t - \phi y_{t-1}\\ &= \mu(1-\phi) + \omega(X_t - \phi X_{t-1}) + \epsilon_t\\ &= \mu(1-\phi) + \omega\left[\frac{t - \phi(t-1)}{12}\right] + \epsilon_t\\ &= \mu(1-\phi) + \frac{\omega\phi}{12} + \frac{\omega(1-\phi)t}{12} + \epsilon_t\\ &= \mu^\star + \omega t^\star + \epsilon_t\end{aligned} \tag{A6}$$

where $\mu^\star = \mu(1-\phi) + \frac{\omega\phi}{12}$ and $t^\star = \frac{(1-\phi)t}{12}$. Thus, in the transformed model, the noise term N_t has been removed. The transformed DLR $y_t{}^\star$ is shown in Figure A1.

According to the weighted least squares estimation:

$$\hat{\omega} = \frac{\sum_{t=1}^T W_t\left(t^\star - \overline{t^\star}\right) y_t{}^\star}{\sum_{t=1}^T W_t\left(t^\star - \overline{t^\star}\right)^2} = \frac{\sum_{t=1}^T W_t\left(t-\bar{t}\right) y_t{}^\star}{\frac{1-\phi}{12}\sum_{t=1}^T W_t\left(t-\bar{t}\right)^2} \tag{A7}$$

where W_t represents the weights determined according to Equation 4, $\overline{y_t{}^\star} = \frac{\sum_{t=1}^T W_t y_t{}^\star}{\sum_{t=1}^T W_t}$, $\overline{t^\star} = \frac{\sum_{t=1}^T W_t t^\star}{\sum_{t=1}^T W_t}$, and $\bar{t} = \frac{\sum_{t=1}^T W_t t}{\sum_{t=1}^T W_t}$.

The variance of the estimated ω:

$$\begin{aligned}\sigma_{\hat{\omega}}{}^2 = Var(\hat{\omega}) &= Var\left[\frac{\sum_{t=1}^T W_t\left(t-\bar{t}\right) y_t{}^\star}{\frac{1-\phi}{12}\sum_{t=1}^T W_t\left(t-\bar{t}\right)^2}\right] = \frac{Var\left[\sum_{t=1}^T W_t\left(t-\bar{t}\right) y_t{}^\star\right]}{\left(\frac{1-\phi}{12}\right)^2\left[\sum_{t=1}^T W_t\left(t-\bar{t}\right)^2\right]^2}\\ &= \frac{Var\left[\sum_{t=1}^T W_t\left(t-\bar{t}\right)\epsilon_t\right]}{\left(\frac{1-\phi}{12}\right)^2\left[\sum_{t=1}^T W_t\left(t-\bar{t}\right)^2\right]^2} = \frac{\sum_{t=1}^T [Var[W_t\left(t-\bar{t}\right)\epsilon_t]]}{\left(\frac{1-\phi}{12}\right)^2\left[\sum_{t=1}^T W_t\left(t-\bar{t}\right)^2\right]^2}\\ &= \frac{Var(\epsilon_t)\sum_{t=1}^T W_t{}^2\left(t-\bar{t}\right)^2}{\left(\frac{1-\phi}{12}\right)^2\left[\sum_{t=1}^T W_t\left(t-\bar{t}\right)^2\right]^2} = \frac{\sigma_\epsilon{}^2\sum_{t=1}^T W_t{}^2\left(t-\bar{t}\right)^2}{\left(\frac{1-\phi}{12}\right)^2\left[\sum_{t=1}^T W_t\left(t-\bar{t}\right)^2\right]^2}\end{aligned} \tag{A8}$$

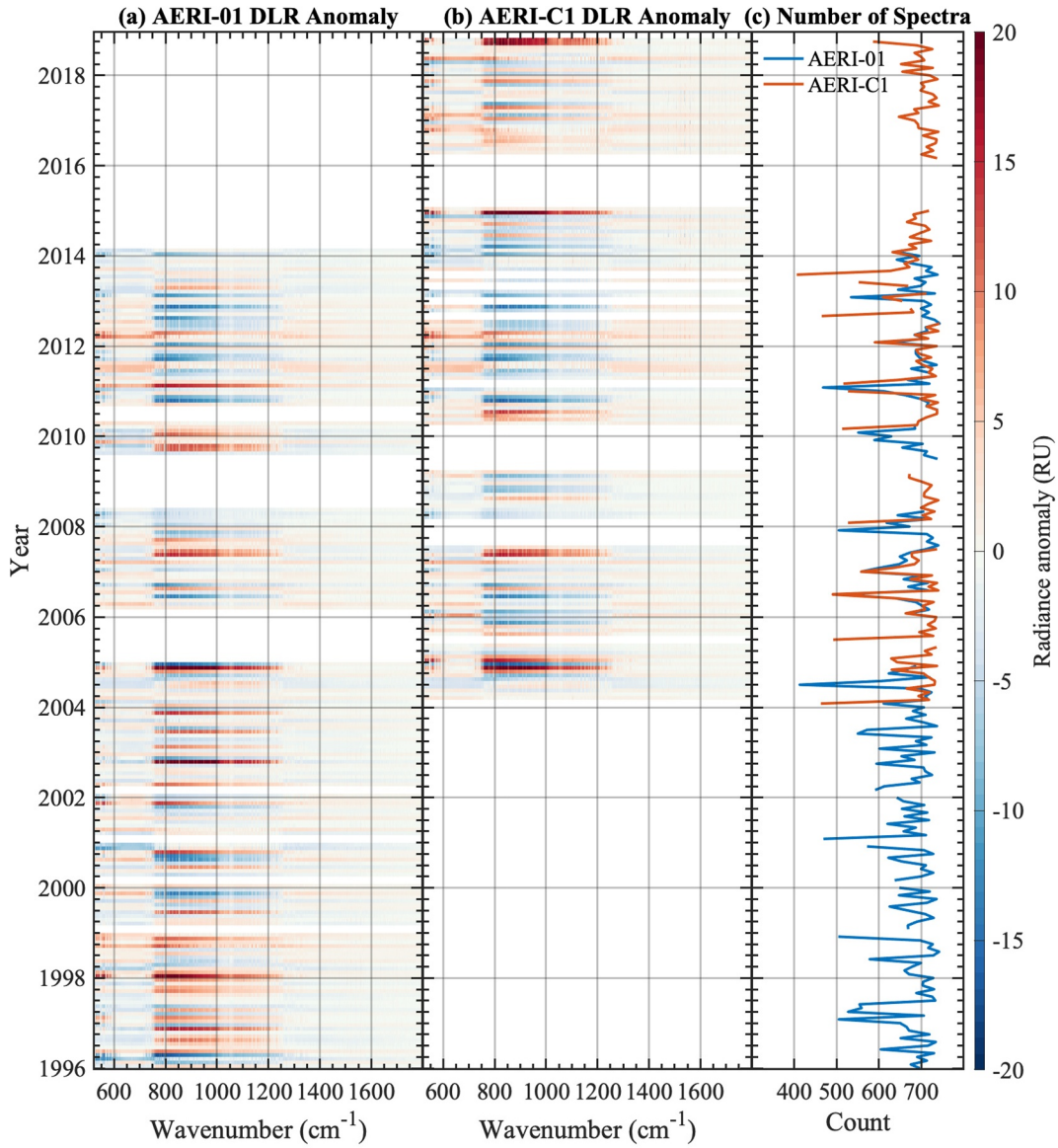

Figure A1. Transformed monthly anomaly of AERI-observed DLR spectra based on Equation A6 and hourly spectra count in each month.

$$\sigma_{\hat{\omega}} = \frac{\sigma_\epsilon}{\frac{1-\phi}{12}} \frac{\sqrt{\sum_{t=1}^{T} W_t^2 \left(t-\bar{t}\right)^2}}{\sum_{t=1}^{T} W_t \left(t-\bar{t}\right)^2} = \sigma_N g(T,\phi,W) \tag{A9}$$

In Equation A9, g is a function of T, ϕ, and W with the explicit expression shown in Equation A10.

$$g(T,\phi,W) = 12\sqrt{\frac{1+\phi}{1-\phi}} \frac{\sqrt{\sum_{t=1}^{T} W_t^2 \left(t-\bar{t}\right)^2}}{\sum_{t=1}^{T} W_t \left(t-\bar{t}\right)^2} \tag{A10}$$

Thus,

$$\sigma_{\hat{\omega}} = 12\,\sigma_N \sqrt{\frac{1+\phi}{1-\phi}} \frac{\sqrt{\sum_{t=1}^{T} W_t^2 \left(t-\bar{t}\right)^2}}{\sum_{t=1}^{T} W_t \left(t-\bar{t}\right)^2} \tag{A11}$$

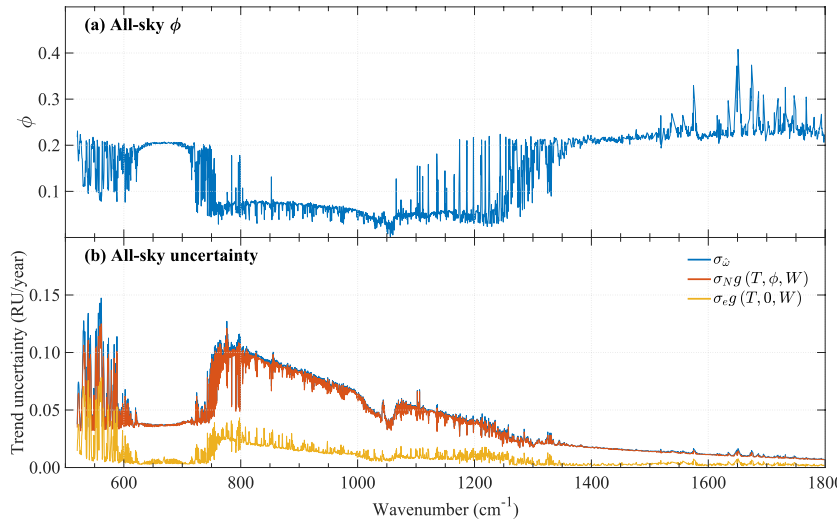

Figure A2. Parameters concerning the radiance trends. (a) The all-sky autocorrelation coefficient based on an AR1 process; (b) All-sky DLR trend uncertainty decomposition based on Equation A14. The blue line represents the total all-sky trend magnitude uncertainty, while the orange and yellow lines represent the all-sky trend magnitude uncertainty arising from natural climate variability and measurement error respectively.

From Equation A11, we conclude that the trend uncertainty is affected by the length of the available data, the natural variability in the data, the autocorrelation of the data, and the derived weights.

A.3. Effect of Measurement Error

When we consider the instrumentation errors e_t in the measurements, Equation A2 becomes:

$$y_t = \mu + \omega X_t + N_t + e_t, t = 1, \cdots, T \tag{A12}$$

e_t is considered to be white noise with zero mean and common variance ${\sigma_e}^2$, $e_t \sim W\left(0, {\sigma_e}^2\right)$, and is considered independent of N_t because N_t originates from unobserved or unsuspected atmospheric factors, while e_t comes from the instrument itself.

In this case, the variance of noise comes from two parts:

$$\sigma^2 = {\sigma_N}^2 + {\sigma_e}^2 \tag{A13}$$

Similar to the derivation in Equation A9, the variance of the estimated trend magnitude is:

$$\begin{aligned}
{\sigma_{\hat{\omega}}}^2 &= {\sigma_N}^2 g^2(T, \phi, W) + {\sigma_e}^2 g^2(T, 0, W) \\
&= {\sigma_N}^2 \frac{1+\phi}{1-\phi} \frac{144 \sum_{t=1}^{T} W_t^2 \left(t - \bar{t}\right)^2}{\left[\sum_{t=1}^{T} W_t \left(t - \bar{t}\right)^2\right]^2} + {\sigma_e}^2 \frac{144 \sum_{t=1}^{T} W_t^2 \left(t - \bar{t}\right)^2}{\left[\sum_{t=1}^{T} W_t \left(t - \bar{t}\right)^2\right]^2} \\
&= \left({\sigma_N}^2 \frac{1+\phi}{1-\phi} + {\sigma_e}^2\right) \frac{144 \sum_{t=1}^{T} W_t^2 \left(t - \bar{t}\right)^2}{\left[\sum_{t=1}^{T} W_t \left(t - \bar{t}\right)^2\right]^2}
\end{aligned} \tag{A14}$$

The uncertainty of the all-sky radiance trend magnitude caused by the natural variability and the measurement error are shown in Figure A2b.

A.4. Time to Detect the Trend

The trend detection ω is judged to be real or significantly different from zero at the 95% level if $|\hat{\omega}| > 2\sigma_{\hat{\omega}}$. $\hat{\omega}$ is approximately normally distributed, so $z = \frac{\hat{\omega}-\omega}{\sigma_{\hat{\omega}}}$ follows a standard normal distribution.

$$Pr\left(|\hat{\omega}| > 2\sigma_{\hat{\omega}}\right) = Pr\left(z > 2 - \frac{\omega}{\sigma_{\hat{\omega}}}\right) \tag{A15}$$

To detect a real trend of specified magnitude $|\omega|$, with probability of 90%, requires that $2 - \frac{\omega}{\sigma_{\hat{\omega}}} < -1.3 \Rightarrow \omega > 3.3\sigma_{\hat{\omega}}$.

Thus, the number of years $n^{\star}$ of data required to detect the trend $\hat{\omega}$ which is determined based on 23-year data, assuming that the trend and noise levels do not change relative to the 23-year period, is

$$n^{\star} \approx \frac{3.3\sigma_{\hat{\omega}}}{|\hat{\omega}|} \times 23\ years \tag{A16}$$

We note that the T2D estimation is different from ascertaining whether the trend magnitude measured from data is significantly different from zero. Hence, although in some channels the trend magnitude is assessed to be "significant", the estimated T2D may be longer than the record length (23 years). This is because when estimating T2D we recognize that the measured time series is one of the many possible realizations that, although governed by the same physical processes and thus of the same true trend, may not render the same trend magnitude in the data. This explains why the factor (3.3) used in the T2D estimation is different from that (2.0) used in the trend significance test.

Appendix B: Homogenization of the Two AERI Records

B.1. Comparison Between the Two AERIs

During the overlapping observation period, the all-sky monthly mean radiance difference between AERI-01 and AERI-C1 is shown in Figure B1. Since these two instruments have different sampling frequency, the AERI-C1 spectra are averaged to match the sampling of AERI-01 spectra before the comparison. From Figure B1a, there

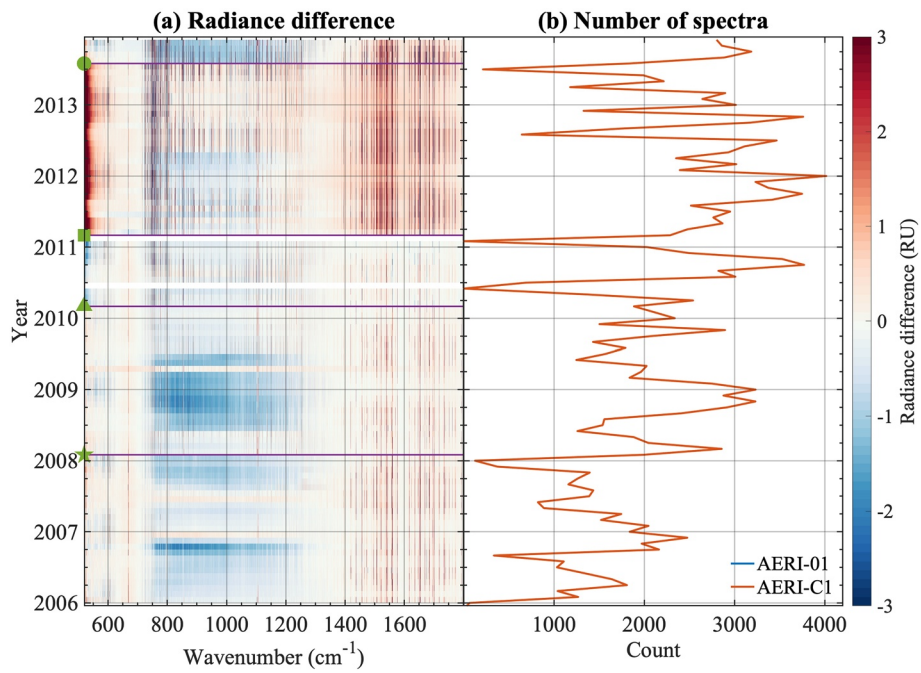

Figure B1. (a) The monthly mean DLR difference between AERI-C1 and AERI-01 (AERI-C1–AERI-01). The green symbols indicate AERI-C1 instrument transitions; (b) Number of 8 min spectra for each month (the counts are identical after AERI-C1 spectra are resampled to match AERI-01).

are noticeable discrepancies between the AERI-01 and AERI-C1 observations. Because of the different sampling frequency, the two AERIs have random errors of different amplitudes (Turner et al., 2006). However, we find that removing the random errors using the principal component analysis following Turner et al. (2006) has little impact on the discrepancies (not shown). We find that in more than 20% of the AERI channels in the spectral range from 700 to 1300 cm^{-1} and for more than 12% of the overlapping observational months, the radiance difference between two AERIs is larger than the documented absolute calibration uncertainty (Knuteson et al., 2004a).

For the AERI-C1 data stream, multiple instruments were used. All these transitions can be seen in Figure B1a as either subtle changes or obvious differences. First, the transition from AERI-04 to AERI-05 happened in September 2009, which caused subtle changes and is labeled by the green star in Figure B1a. These AERIs were among the several AERIs constructed by the University of Wisconsin–Madison for the ARM program. Next, in March 2010, the instrument changed from AERI-05 to AERI-06, which is labeled by the green triangle in Figure B1a. Then, the transition from AERI-06 to AERI-106 happened in March 2011, which caused more noticeable changes and is labeled by the green square in Figure B1a. At this point, the AERI technology was licensed to a commercial vendor, and their units are now characterized by a three-digit number. So AERI-106 is the 6th unit constructed by the vendor. AERI-106 operated until July 2013, when it was replaced with the AERI-108 which has operated at the SGP site since then. We find that the radiance differences between all of these "AERI-C1" instruments and the AERI-01 have unique spectral signatures.

When separating the measured spectra by different sky conditions, we find that the prominent difference between the two AERIs in the window band mainly comes from relatively clear sky conditions. Figure B2 shows the monthly mean radiance difference for different sky conditions in October 2006 as an example. Here the DLR at 985 cm^{-1} is used to classify the sky to be relatively clear or optically thin clouds (<40 RU) or relatively cloudy (>40 RU). We chose 40 RU based on the threshold that Turner and Gero (2011) used to classify cloudy sky to be thin or thick clouds scenes.

We examined various instrumental parameters recorded with AERI measurements, including calibration blackbody temperatures and instrument responsivity, but found that no instrumental parameter explains the radiance difference between the two AERIs. It is possible that an unknown obstruction was partially in the FOV of one of the AERIs (e.g., unit AERI-106), such as what was experienced with an early AERI at the SGP site (Knuteson et al., 1999).

B.2. Clear-Sky LBLRTM Simulations

Since the differences between two AERIs mainly come from relatively clear sky scenes, we use clear sky synthetic spectra simulated by the LBLRTM as a metric to distinguish their relative accuracies. Here we use the classical backpropagation gradient-descent classification algorithm mentioned in Subsection 2.2 to select clear-sky spectra. To ensure the case is clear, we set the algorithm threshold to be 0.8, which means the probability of the sky being clear is at least 0.8.

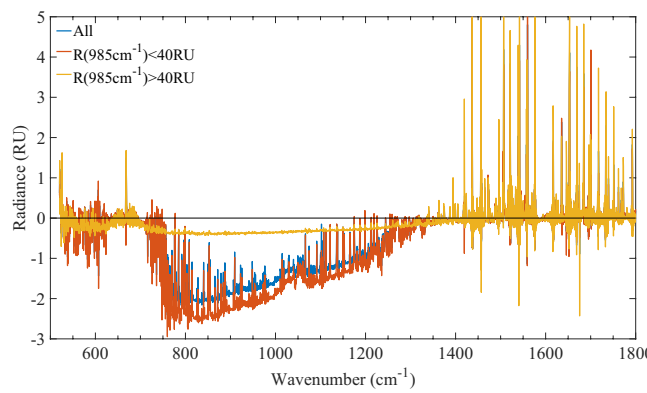

Figure B2. The monthly mean DLR difference between AERI-C1 and AERI-01 (AERI-C1–AERI-01) for different sky conditions in October 2006. See text for details.

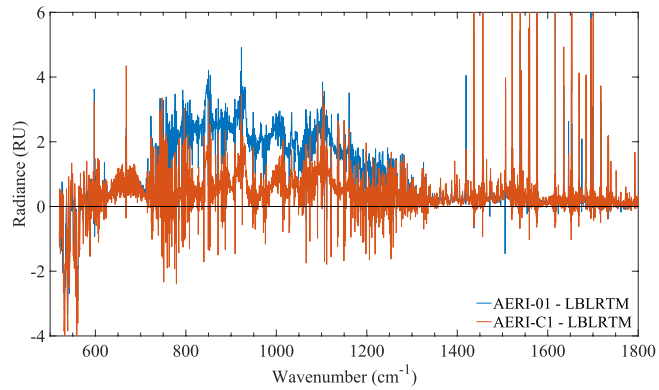

Figure B3. The clear-sky monthly mean DLR difference between AERI-observations and LBLRTM simulations in October 2006.

After matching all datasets, including radiosondes and gas concentrations at SGP mentioned in Section 2.3 to select atmospheric profiles, clear sky synthetic spectra are obtained during the overlapping observational period. For each month, about 70 DLR spectra are simulated on average. The LBLRTM simulation is validated based on the test in Feldman et al. (2015). We chose the same time slices selected in Feldman et al. (2015) to simulate the DLR spectrum and we can achieve similar radiative closures between observation and simulation.

We originally used the ozone concentration profile from the Modern-Era Retrospective analysis for Research and Applications Version 2 (MERRA-2, Gelaro et al., 2017) in simulating the synthetic spectra. A relatively poorer radiance closure between AERI-observations and LBLRTM simulations was found in the ozone absorption band near 1040 cm^{-1}(not shown). By comparing the in-situ measurements at SGP (available only at limited times), we find that this is due to poor representation of the near-surface (and hence lower tropospheric) ozone concentration in the MERRA-2 dataset. To address this issue, we vertically scale the ozone profile uniformly to achieve an improved radiance closure in the ozone band as exemplified by Figure B3 (AERI-C1 line); however, this change to the ozone absorption region between 1040 and 1140 cm^{-1} has little impact on the all-sky radiance trend detected in Figure 5.

As demonstrated in Figure B3, we find that the AERI-C1 is generally in better agreement with LBLRTM simulations than AERI-01, especially in the window band. The radiance difference in each channel is used to weight the spectra of AERI-01 and AERI-C1, according to Equation 2, allowing us to develop an integrated record of monthly mean DLR spectra from the two instruments.

Figure B4 shows the comparison between LBLRTM simulated clear-sky DLR trends (blue dots) and AERI-observed clear-sky DLR trends (red dots) over the 23-year period. The clear-sky DLR trends using simulated clear-sky DLR values are similar to the clear-sky DLR trends using AERI-observations indicating the reliability of the simulated DLR long-term record.

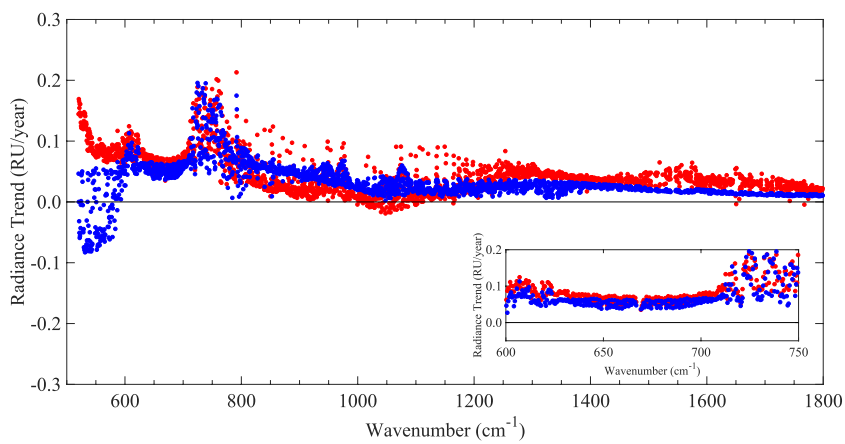

Figure B4. Comparison between LBLRTM simulated clear-sky DLR trends (blue dots) and AERI-observed clear-sky DLR trends (red dots) over the 23-year period. The inset shows the zoomed-in comparison in the CO_2 absorption band.

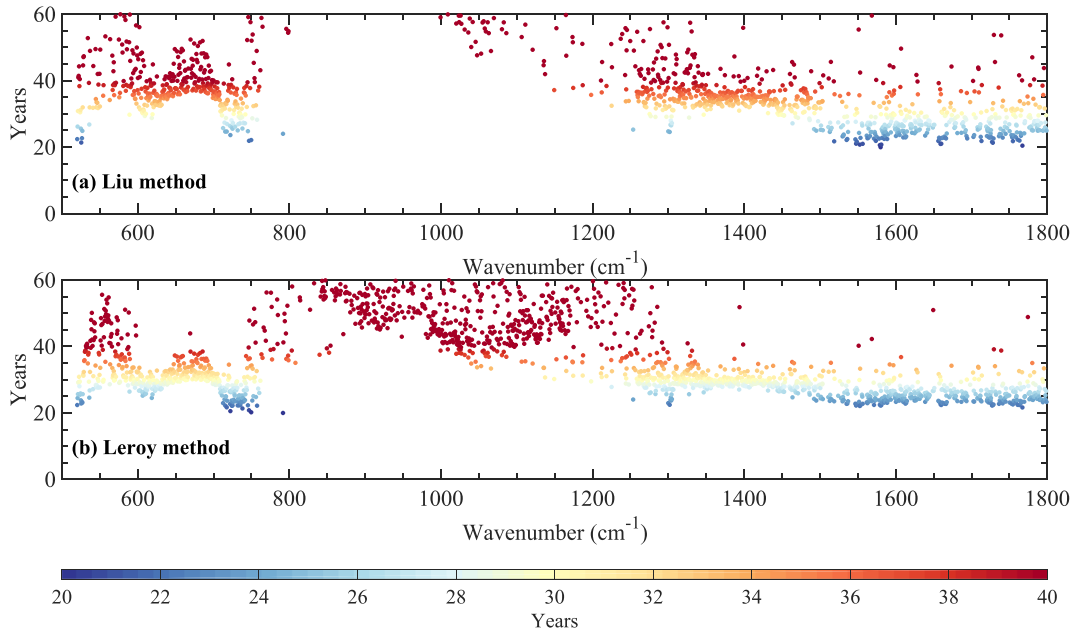

Figure C1. Trend detectability comparison between using (a) the Liu method and (b) the Leroy method.

Appendix C: Comparison of the Estimations of Time to Detect Radiance Trends

Leroy et al. (2008) proposed a formula (hereinafter referred to as the Leroy method) to calculate the minimum time to detect (T2D) a trend. T2D calculated using Equation 6 (hereinafter referred to as the Liu method) is longer than using the Leroy method.

Figure C1 shows the time to detect (T2D) radiance trends at 90% significance level in different AERI channels using the Liu method and the Leroy method respectively. The signal-to-noise ratio s in Equation 11 of Leroy et al. (2008) is set to be 3.3 in order to be consistent with our derivation in Appendix A.4; the terms σ_{var} and σ_{mean} in this equation correspond to σ_N and σ_e in Equation 5 respectively.

The correlation coefficient between T2Ds obtained from the two methods is 0.93. T2D calculated using the Liu method is generally longer than that calculated using the Leroy method by 10 years when T2D is 40 years, and by 45 years when T2D is 100 years.

Data Availability Statement

The original AERI data can be obtained from the ARM data repository (http://www.arm.gov). Our processed monthly mean AERI spectra are available from Mendeley Data (https://data.mendeley.com/datasets/hdwf-m3zpd8/2). CarbonTracker CT2019 B results are provided by NOAA GML, Boulder, Colorado, USA from the website at http://carbontracker.noaa.gov. CarbonTracker-CH4 results are provided by NOAA ESRL, Boulder, Colorado, USA from the website at http://www.esrl.noaa.gov/gmd/ccgg/carbontracker-ch4/.

Acknowledgments
This work is supported by grants from the Fonds de Recherché Nature et Technologies of Quebec (2021-PR-283823) and the Canadian Space Agency (19FAMCGB16). We would like to thank John Brown of NOAA GSL for comments on an earlier version of this manuscript and Lucas Vargas Zeppetello and two anonymous reviewers for their constructive review comments. LL acknowledges the support of a Dr. and Mrs. Milton Leong Graduate Fellowship of McGill University.

References

Brindley, H., & Bantges, R. (2016). The spectral signature of recent climate change. *Current Climate Change Reports*, *2*(3), 112–126. https://doi.org/10.1007/s40641-016-0039-5

Clough, S. A., Shephard, M. W., Mlawer, E. J., Delamere, J. S., Iacono, M. J., Cady-Pereira, K., et al. (2005). Atmospheric radiative transfer modeling: A summary of the AER codes. *Journal of Quantitative Spectroscopy and Radiative Transfer*, *91*(2), 233–244. https://doi.org/10.1016/j.jqsrt.2004.05.058

Cunningham, P., & Delany, S. J. (2020). *k-Nearest neighbour classifiers: (with Python examples)*. *arXiv preprint arXiv:2004.04523*.

Feldman, D. R., Collins, W. D., Gero, P. J., Torn, M. S., Mlawer, E. J., & Shippert, T. R. (2015). Observational determination of surface radiative forcing by CO_2 from 2000 to 2010. *Nature*, *519*(7543), 339–343. https://doi.org/10.1038/nature14240

Gelaro, R., McCarty, W., Suárez, M. J., Todling, R., Molod, A., Takacs, L., et al. (2017). The modern-era retrospective analysis for research and applications, version 2 (MERRA-2). *Journal of Climate*, *30*(14), 5419–5454. https://doi.org/10.1175/jcli-d-16-0758.1

Gero, P. J., & Turner, D. D. (2011). Long-term trends in downwelling spectral infrared radiance over the U.S. Southern Great Plains. *Journal of Climate*, *24*(18), 4831–4843. https://doi.org/10.1175/2011jcli4210.1

Harries, J. E., Brindley, H. E., Sagoo, P. J., & Bantges, R. J. (2001). Increases in greenhouse forcing inferred from the outgoing longwave radiation spectra of the Earth in 1970 and 1997. *Nature*, *410*(6826), 355–357. https://doi.org/10.1038/35066553

Hersbach, H., Bell, B., Berrisford, P., Hirahara, S., Horányi, A., Muñoz-Sabater, J., et al. (2020). The ERA5 global reanalysis. *Quarterly Journal of the Royal Meteorological Society*, *146*(730), 1999–2049. https://doi.org/10.1002/qj.3803

Holdridge, D. (2020). *Balloon-borne sounding System (SONDE) instrument handbook*. In R. Stafford (Ed.), (Ed.). U.S. Department of Energy. DOE/SC-ARM/TR-029.

Huang, Y. (2013). A simulated climatology of spectrally decomposed atmospheric infrared radiation. *Journal of Climate*, *26*(5), 1702–1715. https://doi.org/10.1175/jcli-d-12-00438.1

Huang, Y., Chou, G., Xie, Y., & Soulard, N. (2019). Radiative control of the interannual variability of Arctic sea ice. *Geophysical Research Letters*, *46*(16), 9899–9908. https://doi.org/10.1029/2019gl084204

Huang, Y., Leroy, S. S., & Anderson, J. G. (2010). Determining longwave forcing and feedback using infrared spectra and GNSS radio occultation. *Journal of Climate*, *23*(22), 6027–6035. https://doi.org/10.1175/2010jcli3588.1

Huang, Y., & Ramaswamy, V. (2009). Evolution and trend of the outgoing longwave radiation spectrum. *Journal of Climate*, *22*(17), 4637–4651. https://doi.org/10.1175/2009jcli2874.1

Huang, Y., Ramaswamy, V., Huang, X., Fu, Q., & Bardeen, C. (2007). A strict test in climate modeling with spectrally resolved radiances: GCM simulation versus AIRS observations. *Geophysical Research Letters*, *34*(24). https://doi.org/10.1029/2007gl031409

Huang, Y., Ramaswamy, V., & Soden, B. (2007). An investigation of the sensitivity of the clear-sky outgoing longwave radiation to atmospheric temperature and water vapor. *Journal of Geophysical Research*, *112*(D5). https://doi.org/10.1029/2005jd006906

Jacobson, A. R., Schuldt, K. N., Miller, J. B., Oda, T., Tans, P., Arlyn, A., et al. (2020). *CarbonTracker CT2019B*. Retrieved from https://www.esrl.noaa.gov/gmd/ccgg/carbontracker/CT2019B/

Kapsch, M.-L., Graversen, R. G., Tjernström, M., & Bintanja, R. (2016). The effect of downwelling longwave and shortwave radiation on Arctic summer sea ice. *Journal of Climate*, *29*(3), 1143–1159. https://doi.org/10.1175/jcli-d-15-0238.1

Knuteson, R., Revercomb, H., Best, F., Ciganovich, N., Dedecker, R., Dirkx, T., et al. (2004a). Atmospheric emitted radiance interferometer. Part I: Instrument design. *Journal of Atmospheric and Oceanic Technology*, *21*(12), 1763–1776. https://doi.org/10.1175/jtech-1662.1

Knuteson, R., Revercomb, H., Best, F., Ciganovich, N., Dedecker, R., Dirkx, T., et al. (2004b). Atmospheric emitted radiance interferometer. Part II: Instrument performance. *Journal of Atmospheric and Oceanic Technology*, *21*(12), 1777–1789. https://doi.org/10.1175/jtech-1663.1

Knuteson, R., Whitney, B., Revercomb, H., & Best, F. (1999). *The history of the University of Wisconsin Atmospheric Emitted Radiance Interferometer (AERI) prototype during the period April 1994 through July 1995*. University of Wisconsin--Madison, Space Science and Engineering Center.

Leroy, S. S., Anderson, J. G., & Ohring, G. (2008). Climate signal detection times and constraints on climate benchmark accuracy requirements. *Journal of Climate*, *21*(4), 841–846. https://doi.org/10.1175/2007jcli1946.1

Liebmann, B., & Smith, C. A. (1996). Description of a complete (interpolated) outgoing longwave radiation dataset. *Bulletin of the American Meteorological Society*, *77*(6), 1275–1277.

Lubin, D. (1994). The role of the tropical super greenhouse effect in heating the ocean surface. *Science*, *265*(5169), 224–227. https://doi.org/10.1126/science.265.5169.224

Palchetti, L., Brindley, H., Bantges, R., Buehler, S., Camy-Peyret, C., Carli, B., et al. (2020). Unique far-infrared satellite observations to better understand how Earth radiates energy to space. *Bulletin of the American Meteorological Society*, *101*(12), E2030–E2046. https://doi.org/10.1175/bams-d-19-0322.1

Pan, F., Huang, X., Strow, L. L., & Guo, H. (2015). Linear trends and closures of 10-yr observations of AIRS stratospheric channels. *Journal of Climate*, *28*(22), 8939–8950. https://doi.org/10.1175/jcli-d-15-0418.1

Peters, W., Jacobson, A. R., Sweeney, C., Andrews, A. E., Conway, T. J., Masarie, K., et al. (2007). An atmospheric perspective on North American carbon dioxide exchange: CarbonTracker. *Proceedings of the National Academy of Sciences*, *104*(48), 18925–18930. https://doi.org/10.1073/pnas.0708986104

Revercomb, H. E., Buijs, H., Howell, H. B., LaPorte, D. D., Smith, W. L., & Sromovsky, L. (1988). Radiometric calibration of IR Fourier transform spectrometers: Solution to a problem with the High-Resolution Interferometer Sounder. *Applied Optics*, *27*(15), 3210–3218. https://doi.org/10.1364/ao.27.003210

Revercomb, H. E., Turner, D. D., Tobin, D., Knuteson, R. O., Feltz, W., Barnard, J., et al. (2003). The ARM program's water vapor intensive observation periods: Overview, initial accomplishments, and future challenges. *Bulletin of the American Meteorological Society*, *84*(2), 217–236. https://doi.org/10.1175/bams-84-2-217

Rowe, P. M., Neshyba, S. P., Cox, C. J., & Walden, V. P. (2011). A responsivity-based criterion for accurate calibration of FTIR emission spectra: Identification of in-band low-responsivity wavenumbers. *Optics Express*, *19*(7), 5930–5941. https://doi.org/10.1364/oe.19.005930

Rowe, P. M., Neshyba, S. P., & Walden, V. P. (2011). Responsivity-based criterion for accurate calibration of FTIR emission spectra: Theoretical development and bandwidth estimation. *Optics Express*, *19*(6), 5451–5463. https://doi.org/10.1364/oe.19.005451

Shupe, M. D., & Intrieri, J. M. (2004). Cloud radiative forcing of the Arctic surface: The influence of cloud properties, surface albedo, and solar zenith angle. *Journal of Climate*, *17*(3), 616–628. https://doi.org/10.1175/1520-0442(2004)017<0616:crfota>2.0.co;2

Sokolowsky, G. A., Clothiaux, E. E., Baggett, C. F., Lee, S., Feldstein, S. B., Eloranta, E. W., et al. (2020). Contributions to the surface downwelling longwave irradiance during Arctic Winter at Utqiaġvik (Barrow), Alaska. *Journal of Climate*, *33*(11), 4555–4577. https://doi.org/10.1175/jcli-d-18-0876.1

Stephens, G. L., Li, J., Wild, M., Clayson, C. A., Loeb, N., Kato, S., et al. (2012). An update on Earth's energy balance in light of the latest global observations. *Nature Geoscience*, *5*(10), 691–696. https://doi.org/10.1038/ngeo1580

Tiao, G. C., Reinsel, G. C., Xu, D., Pedrick, J., Zhu, X., Miller, A., et al. (1990). Effects of autocorrelation and temporal sampling schemes on estimates of trend and spatial correlation. *Journal of Geophysical Research: Atmospheres*, *95*(D12), 20507–20517. https://doi.org/10.1029/jd095id12p20507

Trenberth, K. E., Fasullo, J. T., & Kiehl, J. (2009). Earth's global energy budget. *Bulletin of the American Meteorological Society*, *90*(3), 311–324. https://doi.org/10.1175/2008bams2634.1

Turner, D., Knuteson, R., Revercomb, H., Lo, C., & Dedecker, R. (2006). Noise reduction of Atmospheric Emitted Radiance Interferometer (AERI) observations using principal component analysis. *Journal of Atmospheric and Oceanic Technology*, *23*(9), 1223–1238. https://doi.org/10.1175/jtech1906.1

Turner, D. D., & Gero, P. J. (2011). Downwelling 10μm radiance temperature climatology for the Atmospheric Radiation Measurement Southern Great Plains site. *Journal of Geophysical Research*, *116*(D8). https://doi.org/10.1029/2010jd015135

Turner, D. D., Lesht, B. M., Clough, S. A., Liljegren, J. C., Revercomb, H. E., & Tobin, D. (2003). Dry bias and variability in Vaisala RS80-H radiosondes: The ARM experience. *Journal of Atmospheric and Oceanic Technology*, *20*(1), 117–132. https://doi.org/10.1175/1520-0426(2003)020<0117:dbaviv>2.0.co;2

Turner, D. D., Tobin, D., Clough, S. A., Brown, P. D., Ellingson, R. G., Mlawer, E. J., et al. (2004). The QME AERI LBLRTM: A closure experiment for downwelling high spectral resolution infrared radiance. *Journal of the Atmospheric Sciences*, *61*(22), 2657–2675. https://doi.org/10.1175/jas3300.1

Wang, J., Cole, H. L., Carlson, D. J., Miller, E. R., Beierle, K., Paukkunen, A., & Laine, T. K. (2002). Corrections of humidity measurement errors from the Vaisala RS80 radiosonde—Application to TOGA COARE data. *Journal of Atmospheric and Oceanic Technology*, *19*(7), 981–1002. https://doi.org/10.1175/1520-0426(2002)019<0981:cohmef>2.0.co;2

Weatherhead, E. C., Reinsel, G. C., Tiao, G. C., Meng, X.-L., Choi, D., Cheang, W.-K., et al. (1998). Factors affecting the detection of trends: Statistical considerations and applications to environmental data. *Journal of Geophysical Research*, *103*(D14), 17149–17161. https://doi.org/10.1029/98jd00995

Wielicki, B. A., Wong, T., Allan, R. P., Slingo, A., Kiehl, J. T., Soden, B. J., et al. (2002). Evidence for large decadal variability in the tropical mean radiative energy budget. *Science*, *295*(5556), 841–844. https://doi.org/10.1126/science.1065837

Wild, M., Folini, D., Schär, C., Loeb, N., Dutton, E. G., & König-Langlo, G. (2012). The global energy balance from a surface perspective. *Climate Dynamics*, *40*(11–12), 3107–3134. https://doi.org/10.1007/s00382-012-1569-8